Tribol Lett (2014) 56:355–374
DOI 10.1007/s11249-014-0414-0

ORIGINAL PAPER

Effects of Interfacial Strength and Roughness on the Static Friction Coefficient

Deepak B. Patil · Melih Eriten

Received: 25 June 2014 / Accepted: 13 September 2014 / Published online: 23 September 2014

Abstract A finite element model is used to simulate sliding inception of a rigid flat on a deformable sphere under combined normal and tangential loading. Sliding inception is treated as the loss of tangential contact stiffness under combined effects of plasticity, crack propagation and interfacial slip. Energy dissipation distribution is used to quantify the relative contribution of these mechanisms on the increased compliance during tangential loading. Materials with different strength and toughness properties, and varying local interface conditions ranging from fully adhered to finite friction, are studied to relate variations in plastic deformations, crack and slip to the sliding inception. For fully adhered contact condition, crack and fracture toughness have no effect on sliding inception, with plasticity, the dominant failure mechanism. A measure of recoverable strain (yield strength to Young's modulus ratio) is found to be the most influential parameter in sliding inception. Interfacial slip is expectedly the dominant mechanism for sliding inception for lower coefficient of friction, modeling lubricated contacts. Interplay of plasticity and interfacial slip is found to govern the onset of sliding for higher local friction coefficients. Furthermore, the single asperity results are incorporated in a statistical model for nominally flat contacting rough surfaces under combined normal and tangential loading to investigate the stochastic effects due to surface roughness and material property uncertainties. The results show that the static coefficient of friction strongly depends on the normal load, material properties, local interfacial strength and roughness parameters.

Keywords Static friction · Interfacial strength · Spherical contact · Rough surfaces · Uncertainties in frictional contacts

1 Introduction

Understanding the onset of sliding and thereby accurately predicting static coefficient of friction would have benefits for a wide range of applications. Cattaneo [1] and Mindlin [2] pioneered in addressing the problem of elastic spheres under combined normal and tangential loading. Under fully adhered contact conditions, their formulations led to interfacial shear traction with singularities at the contact edges. Since no material can withstand infinite shear tractions, they suggested local interfacial slip as the stress relaxation mechanism and concluded that the accumulation and coalescence of local interfacial slip would lead to global sliding. Many studies including and following the Cattaneo–Mindlin approach assumed local Coulomb friction governing the interfacial slip. This assumption combined with fully elastic material response, however, resulted in the classical Coulomb friction law, where the onset of sliding occurred at tangential loads directly proportional to the normal loads with a proportionality constant known as friction coefficient. In other words, by choosing a local friction coefficient to govern the interfacial slip, one automatically sets the overall frictional strength of the contact to the same value. See Ref. [3] for a critical review of these assumptions.

An alternative to Cattaneo–Mindlin approach was devised by others [4, 5], where sliding inception was linked

D. B. Patil · M. Eriten (✉)
Department of Mechanical Engineering, University of Wisconsin – Madison, 1513 University Avenue, Madison, WI 53706, USA
e-mail: eriten@wisc.edu

to various interfacial strength properties. Among these properties were the type and strength of bonds formed at the contact and their rupture, and the strength of contacting materials against shearing. Following this approach, various researchers have carried out experimental and numerical studies and showed that material yielding was prominent in onset of sliding [6–11]. Recently, Fineberg and his group focused on interfacial rupture to explain the onset of sliding [12–15]. They conducted experimental studies and observed that the waves of rupture events triggered the onset of sliding. These waves could be attributed to the rupture of asperity-scale contacts. Eriten et al. [16] developed a physics-based model to explain partial slip for a spherical contact. This model integrated the Cattaneo–Mindlin approach with friction coefficient values based on material yielding rather than using local Coulomb friction coefficient. Wu et al. [17] based the onset of sliding on maximum frictional shear stress criterion. According to this model, the shear strength of the weaker material was set as the critical frictional shear stress, and once the frictional shear stress in the contact area reaches the limiting shear strength, local sliding occurs at that point. A recent paper by Mulvihill et al. [18] looked at interface adhesion shear strength and plasticity to explain the sliding friction coefficient. They conclude that the sliding friction coefficient arises from both plasticity and tangential interface adhesion.

The onset of sliding at the asperity scale depends on material strength and toughness as well as interfacial slip. However, in practice, surfaces are rough. The statistical summation approach by Greenwood and Williamson [19] has been one of the frequently used methods to extend the asperity-scale contact formulations to rough surface scale in the above studies. Kogut and Etsion [20] extended their work in Ref. [7] to predict the static coefficient of friction at rough surface. Cohen et al. [21] proposed a model for static friction based on the full stick asperity-scale model by Brizmer et al. [6]. This study was extended further for higher plasticity index [19] values by Li et al. [22]. Eriten et al. [23] successfully implemented the asperity-scale models in Ref. [16] at the rough surface scale to explain fretting behavior in mechanical lap joints. These studies show that roughness parameters such as plasticity index and asperity height distribution [24] influence the static friction coefficient at macroscale contacts. Asperity height distribution is shown to influence the energy dissipation in cyclic tangential loading of an elastic contact [25] and affect the real contact area and contact load during normal loading [22, 26].

The current model differs from the previous works by studying the interlink among the major mechanisms viz interfacial slip, material yielding and crack on the onset of sliding at the asperity scale using finite element simulations. Further, the results from the asperity-scale model are extended to the rough surface scale using the Greenwood–Williamson [19] statistical summation approach to include the stochastic effects of roughness parameters (plasticity index and asperity height distributions) on the static coefficient of friction. Section 2 describes both the asperity-scale model and the rough surface model and gives theoretical background of the work presented. Section 3 gives the details of the finite element model (FEM) employed for the asperity-scale formulations. The results obtained are discussed in Sect. 4 followed by conclusions in Sect. 5.

2 Methodology

2.1 Asperity Scale

The asperity-scale contact is modeled as a rigid flat firstly pressed on a deformable sphere by a constant normal load, P, and then sheared tangentially by a tangential force, Q. The application of the normal load causes an initial interference of ω_o, and the subsequent tangential force leads to tangential displacement of u_x. Loading rates are assumed to be low to ensure static conditions hold. Cattaneo–Mindlin's approach to this problem yields the following solution,

$$Q = \mu P\left\{1 - \left(1 - \frac{16au_xG}{3\mu P(2-\nu)}\right)^{3/2}\right\} \tag{1}$$

where G is the shear modulus, ν is the Poisson's ratio, a is contact radius and μ is local friction coefficient. Taking the partial derivative of Eq. (1) with respect to u_x, the tangential contact stiffness, $\partial Q/\partial u_x$ is given by Eq. (2),

$$\frac{\partial Q}{\partial u_x} = \frac{8aG}{2-\nu}\left\{1 - \left(1 - \left(1 - \frac{Q}{\mu P}\right)^{2/3}\right)\right\}^{\frac{1}{2}} \tag{2}$$

The tangential stiffness decreases with increasing tangential load due to interfacial slip. At a limiting tangential load ($Q = \mu P$), the tangential stiffness reaches zero, where the contacting bodies slide against each other [see Eq. (2)]. Approximating $\partial Q/\partial u_x$ for small tangential loads gives the initial tangential contact stiffness as,

$$K_t^0 = \frac{8aG}{(2-\nu)} \tag{3}$$

Interfacial slip is not possible for a fully adhered contact, and hence, material failure (plasticity and fracture) is expected to weaken the contact in tangential response [6, 27]. The ratio of the limiting tangential load and normal load, Q/P is now considered as the static coefficient of friction [6]. In this work, the evolution of tangential load versus tangential displacement will be studied in

elastic–plastic materials with fracture option via an extended finite element model (XFEM) described in Sect. 3. Relative contribution of each failure mechanism to interface weakening and static friction coefficient is quantified with corresponding energy dissipations at the onset of sliding. Since there is no body force and kinetic energy in our XFEM, by the conservation of energy, the rate of change of internal energy is equal to the rate of work done by surface loads,

$$\frac{\mathrm{d}}{\mathrm{d}t}\int_V (\rho U)\mathrm{d}V = \int_S \mathbf{v}.\mathbf{t}\mathrm{d}S \tag{4}$$

Here, ρ is the mass density, $\mathbf{v}$ is the velocity field vector, U is the internal energy per unit mass and $\mathbf{t}$ is the surface traction vector. Integrating Eq. (4) in time, using Cauchy's equation of motion and the relation, $\mathbf{t} = \boldsymbol{\sigma}\cdot\mathbf{n}$, where, $\boldsymbol{n}$ is the normal vector on surface S, we can rewrite the above equation as,

$$\int_o^t \int_V \sigma : \dot{\varepsilon}\mathrm{d}V\mathrm{d}t = \int_0^t \int_S \mathbf{v}.\mathbf{t}\mathrm{d}S\mathrm{d}t \tag{5}$$

Using strain decomposition and splitting the traction vector into frictional traction and traction due to external load, the final expression for the energy balance is given as [28],

$$\begin{aligned}&\int_0^t \int_S \mathbf{v}.\mathbf{t}^l\mathrm{d}S\mathrm{d}t - \int_o^t \int_V \left(\frac{1-d_\mathrm{t}}{1-d}\right)\sigma : \dot{\varepsilon}^{el}\mathrm{d}V\mathrm{d}t \\ &= \int_o^t \int_V \left(\frac{d_\mathrm{t}-d}{1-d}\right)\sigma : \dot{\varepsilon}^{el}\mathrm{d}V\mathrm{d}t + \int_o^t \int_V \sigma : \dot{\varepsilon}^{pl}\mathrm{d}V\mathrm{d}t \\ &\quad + \left(-\int_0^t \int_S \mathbf{v}.\mathbf{t}^f\mathrm{d}S\mathrm{d}t\right)\end{aligned} \tag{6}$$

Here, $\mathbf{t}^l$ is the surface distributed load and $\mathbf{t}^f$ is the frictional traction, σ is the stress tensor, $\dot{\varepsilon}^{el}$ and $\dot{\varepsilon}^{pl}$ are elastic and plastic strain rate tensors, respectively, and d is the damage parameter. The damage parameter $d = 0$ represents an undamaged material and $d = 1$ represents fully damaged material; and d_t is the constant value attained by d at time t upon unloading. The damage parameter d is given by Eq. (7),

$$d = \int_{\delta_\mathrm{m}^o}^{\delta_\mathrm{m}^f} \frac{T_\mathrm{eff}\mathrm{d}\delta}{G_\mathrm{c} - G_\mathrm{o}} \tag{7}$$

Here, T_eff and δ are the effective traction and displacement at the crack interface, respectively, δ_m^o is the effective displacement at initiation of damage and δ_m^f is the effective displacement at complete failure, G_o is the elastic strain energy at damage initiation and G_c is the input fracture energy. The effective traction is computed as the square root of summation of the squares of the components in the normal direction and the two shear directions. The energy balance [Eq. (6)] shows that the total work done by external loads (E_W) minus the recoverable elastic strain energy (E_E) equals to the energy dissipated due to damage (E_D), plasticity (E_P) and friction (E_F), i.e., $E_\mathrm{W} - E_\mathrm{E} + \text{constant} = E_\mathrm{D} + E_\mathrm{P} + E_\mathrm{F}$. XFEM is used to obtain both the evolution of tangential load–displacement and the internal strain–stress fields to evaluate the energy dissipation distribution at the asperity scale.

2.2 Rough Surface Scale

At macroscale, most engineering surfaces are rough and consist of numerous asperities forming the real load-bearing area. One of the methods to extend asperity-scale contact formulations to macroscale is the statistical summation approach proposed in the pioneering work of Greenwood and Williamson (GW) [19]. Statistical summation uses distribution of asperity heights over the nominal contact area, A_n to add the contributions of individual asperities. The GW model assumes the rough surface to be isotropic, and the asperities to have spherical shape with identical radius, R. There is no interaction between the asperities, i.e., they are distributed sufficiently far apart. McCool [29] showed that there is no appreciable loss of generality by relaxing some of the assumptions of GW model. However, GW model cannot completely describe the load-interference relations with bulk deformation and asperity interactions [30]. In this study, the asperity interactions and bulk deformation are ignored and could result in deviations from the standard GW model predictions. The reader is referred to Ref. [29–31] for the applicability of the GW model. McCool [29] also proposed a method to combine the roughness of the two nominally flat rough surfaces into an equivalent rough surface and a rigid flat. The contact of such an equivalent surface with a rigid flat will be used in our rough surface scale formulations (see Fig. 1).

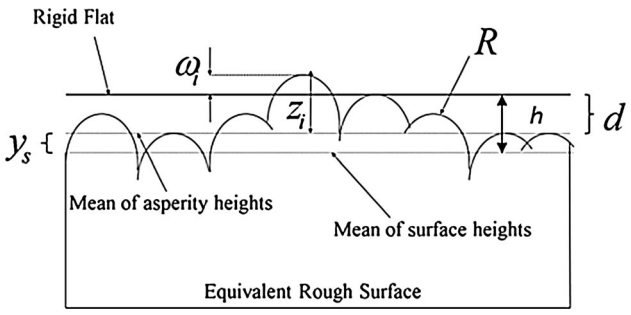

Fig. 1 Schematic representation of an equivalent rough surface and a rigid flat contact [23]

In this formulation, the distance between the rigid flat and the reference plane defined by the mean of asperity heights is denoted by d, and the distance between the mean of surface heights and the rigid flat is denoted as h. The distance between the mean of surface heights and the mean of asperity heights is represented as y_s. The interference, ω, is defined as z-d, where z is the height of the asperity. The load is carried by an asperity when the interference, ω, is positive, i.e., z-d greater than zero. Our model initially assumes normal distribution for the asperity heights (this assumption will be revisited in the results Sect. 4.2.4 to include other types of distribution). The normal distribution is commonly observed in engineering surfaces manufactured by abrasive and/or generic cumulative removal processes [26, 32–34]. For the asperity heights with standard deviation, σ_s, the probability density function for a normal distribution is given by,

$$\phi(z) = \frac{1}{\sqrt{2\pi}\sigma_s}\exp\left(-0.5\left(\frac{z}{\sigma_s}\right)^2\right) \tag{8}$$

The probability density function is normalized to the standard deviation of the surface heights σ and is written in dimensionless form as,

$$\phi^*(z^*) = \frac{1}{\sqrt{2\pi}}\frac{\sigma}{\sigma_s}\exp\left(-0.5\left(\frac{\sigma}{\sigma_s}\right)^2 (z^*)^2\right) \tag{9}$$

where $z^* = \frac{z}{\sigma}$; $\frac{\sigma}{\sigma_s} = \sqrt{1 - \frac{3.717\times10^{-4}}{\beta^2}}$ and $\beta = \eta R\sigma$, where $\eta =$ the area density of the asperities. The separations d, h and y_s are also normalized to σ and can be related using the roughness parameter β as [20],

$$y_s^* = h^* - d^* = \frac{1}{\sqrt{48}\pi\beta} \tag{10}$$

The interference, ω, can be written in dimensionless form as $\omega^* = z^* - d^*$. If no asperity interactions occur, the total normal load on the rigid flat is given by the summation of the normal load carried by each individual asperity, P, with a positive dimensionless interference, ω^*, for a given separation, d^*,

$$P_{\text{flat}} = \eta A_n \int_{d^*}^{\infty} P(z^* - d^*)\phi^*(z^*)\mathrm{d}z^* \tag{11}$$

The load carried by an individual asperity will fall into elastic regime or elastic–plastic regime depending on the asperity height and the interference. Local interfacial conditions change the asperity-scale load formulation slightly. Eriten et al. [16] compared the normal load formulations under fully adhered and frictionless contacts and concluded that friction's effect on the load-penetration response of the spherical contact is negligible. In accordance with this observation, the normal load formulation of frictionless contacts is used in this study irrespective of the contact conditions. Thus, in the elastic regime Hertz's [35], and in the elastic–plastic regime Kogut and Etsion's [36], formulations are used;

$$P_{\text{el}} = P_c\left(\frac{\omega}{\omega_c}\right) \quad \text{for } \omega \le \omega_c \tag{12}$$

$$P_{\text{pl}}^1 = 1.03P_c\left(\frac{\omega}{\omega_c}\right)^{1.425} \quad \text{for } \omega_c \le \omega \le 6\omega_c \tag{13}$$

$$P_{\text{pl}}^2 = 1.4P_c\left(\frac{\omega}{\omega_c}\right)^{1.263} \quad \text{for } 6\omega_c \le \omega \le 110\omega_c \tag{14}$$

where P_c and ω_c are the critical load and critical interference at yielding inception under frictionless condition. The von Mises criterion with the Hertzian stress field gives the critical load and critical interference at yield inception as,

$$P_c = \frac{\pi^3}{6K_v^3}Y\left(R(1-\nu^2)\frac{Y}{E}\right)^2 \tag{15}$$

$$\omega_c = \left(\frac{1}{K_v}\frac{\pi(1-\nu^2)}{2}\frac{Y}{E}\right)^2 R \tag{16}$$

where Y is the virgin yield strength of the material, E is the Young's modulus, ν is the Poisson's ratio and K_v is given by,

$$K_v = \left\{\frac{3}{2}\left(1+\frac{z^2}{a^2}\right)^{-1} - (1+\nu)\left[\left(1-\frac{z}{a}\tan^{-1}\left(\frac{a}{z}\right)\right)\right]\right\} \tag{17}$$

where z/a can be approximated as $z/a = 0.381 + \nu/3$ [37].

From Eqs. (15) and (16), the critical load can be expressed in terms of the critical interference as,

$$P_c = \frac{2\pi}{3K_v}RY\omega_c \tag{18}$$

The plasticity index ψ, a measure of the ratio of the plastically yielded areas to the total contact area for the contact of nominally flat rough surfaces, was introduced by Greenwood and Williamson [19]. The critical interference, ω_c, can be expressed in terms of plasticity index, ψ as,

$$\psi = \frac{E}{H}\sqrt{\frac{\sigma_S}{R}} = \left(\omega_c^*\frac{\sigma}{\sigma_s}\right)^{-0.5} \tag{19}$$

Substituting Eq. (19) into Eq. (18) and further into Eqs. (12–14), and finally in the integral of Eq. (11), the total dimensionless normal load carried by the rigid flat is given by Eq. (30) (see "Appendix").

Similar to the total normal load formulation given in Eq. (11), the maximum tangential load supported by the rigid flat is given by,

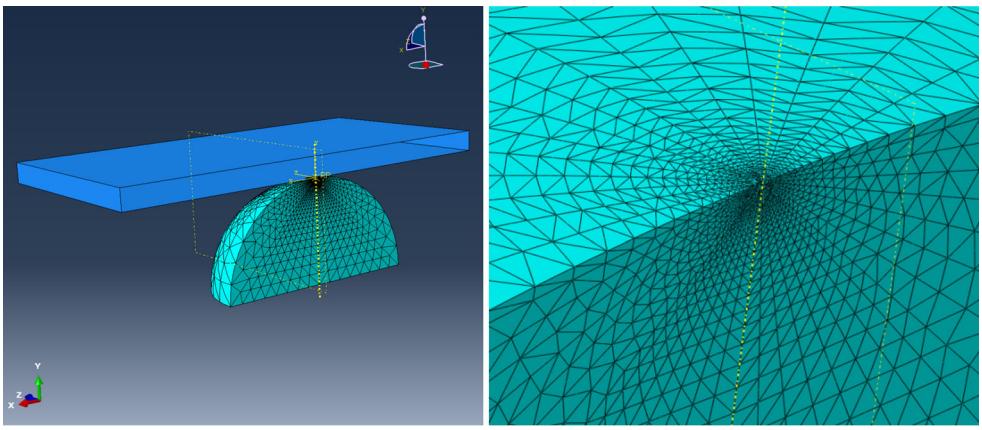

(a) **(b)**

Fig. 2 **a** Finite element model of a rigid flat on a deformable sphere and **b** close-up of mesh near contact

$$Q_{\max-\text{flat}} = \eta A_{\text{n}} \int_{d^{\cdot}}^{\infty} Q_{\max}(z^{\cdot} - d^{\cdot})\phi^{\cdot}(z^{\cdot})\mathrm{d}z^{\cdot} \tag{20}$$

The maximum tangential load an individual asperity can sustain is given by,

$$Q_{\max} = \mu(\omega, E/Y, \mu_{\text{local}})P \tag{21}$$

where P takes the form in Eqs. (12)–(14) and μ is the friction coefficient for each asperity and is a function of the interference, material properties and the local contact friction (local interfacial strength). Physically, the local friction coefficient values indicate the adhesion shear strength of the interface. The friction coefficients at the asperity level will be computed by a XFEM.

3 FE Model

A 3D FEM of a rigid flat on a deformable sphere is developed in ABAQUS 6.12 as shown in Fig. 2.

The FEM consists of 22729 ten-node tetrahedral elements with 35566 nodes for the deformable sphere. The flat is modeled as a rigid body. The mesh is finest nearby the contact and gradually coarsens away from the contact (see Fig. 2). Surface-to-surface contact formulation with penalty method is used to model the contact between the flat and the sphere. The default penalty stiffness set to 10 times the representative underlying element stiffness is chosen to enforce the "Hard" contact in ABAQUS [38–41]. Minimum 16 nodes through the radius are in contact for the lowest normal load applied, and a maximum of 48 nodes are in contact for the largest normal load. The FEM is verified with analytical Hertz solution for normal loading and Mindlin's solution for tangential loading under elastic conditions. The results from frictionless normal loading for load–displacement, contact pressure–contact radius and maximum principal stress at symmetry plane through depth

Table 1 Material properties

Material	E/Y	Elastic modulus, E (GPa)	Yield strength, Y (MPa)	Poisson's ratio, v	Fracture toughness, K_{c} (MPa m$^{1/2}$)
A	85	450	5,200	0.22	3
B	140	116	830	0.3	95
C	250	69	280	0.33	29
D	400	205	515	0.29	50

are all within 5 % of Hertz analytical solution. The initial tangential stiffness results for shear loading are within 8 % of Mindlin's analytical solution [see Eq. (3)]. The energy balance [see Eq. (6)] is verified by a similar model in Fig. 2, albeit with a finer mesh in the annular slip region. The model is subjected to a low cyclic tangential load under elastic conditions [essentially suppressing the first two terms on the right-hand side of Eq. (6)]; the energy dissipated by interfacial slip is within 10 % of Mindlin's analytical solution for energy loss during cyclic tangential loading of the sphere.

The contact between the flat and sphere is considered to be fully adhered initially to give an upper bound on the onset of sliding for the contacting bodies. The contact between the bodies is also set to coefficient of friction 0.2 through 1 later to evaluate the effect of interfacial slip on sliding inception. The lower friction coefficient value of 0.2 is the representative of lubricated contacts, whereas the higher value of 1 models the surfaces with high interfacial strength. The ratio of stick radius to contact radius is given by $c/a = (1 - Q/\mu P)^{1/3}$ [42]. If the ratio of tangential load to normal load is held constant, choosing a friction coefficient of 1 compared to 0.2 increases the percentage of stick region from 88 to 98 %, giving a good variation to study the influence of slip. The deformable sphere is modeled after four different materials, and the details of the

material properties are listed in Table 1 [43–46]. These material properties cover a wide range of yield strength and fracture toughness values and thus enable us to investigate the effects of material strength on the onset of sliding.

The materials are assumed to be linear isotropic elastic and perfect plastic. Von Mises yielding criterion with associated flow is used to model plasticity. The constant normal load is applied to the reference point of the rigid flat at the topmost node of the spherical contact. After the completion of normal loading phase, a gradually increasing tangential load is applied to the rigid flat. The rotation of the flat is disallowed to ensure perfect tangential motion. Each simulation terminates when tangential stiffness of the contacting bodies is less than 10 % of initial tangential stiffness. A typical simulation takes around 2–4 h on a computer with a 3.4 GHz Intel i7-3770 processor and 16 GB of memory.

The FEM also has an XFEM module incorporated in it. This module is turned ON and employed only when simulating the initiation and propagation of cracks during the combined normal and tangential loading of the sphere (for a selected few results described in Sect. 4). The XFEM utilizes local enrichment of nodes through partition of unity. A fracture event is initiated when the chosen damage initiation criterion is satisfied, and the subsequent changes in material response are modeled with a displacement function that is discontinuous across the crack surface [47]. No explicit representation or seeding of cracks is needed. Crack surfaces and tips are entirely described by the nodal data, and special functions accounting for stress intensification at the crack tips. This enables accurate modeling of the crack without the need of remeshing [47]. XFEM is being implemented widely in many studies, particularly for fatigue crack growth simulations [48–50]. While implementing the XFEM in ABAQUS 6.12, cohesive zone model is used. The crack initiation is assumed to occur when maximum principal stress reaches the maximum tensile stress at the end of normal loading (radial stresses close to surface at the contact circumference). The fracture toughness values of the materials listed in Table 1 are converted to energy release rates based on plane stress criterion [see Eq. (22)] and are used to govern the damage evolution [see Eq. (7)].

$$G_c = \frac{K_c^2}{E} \tag{22}$$

where G_c is the energy release rate, K_c is the fracture toughness in mode I and E is the Young's modulus. Analytical finite plate solution for stress intensity factor for a through central crack of total length 1 m in a 4 × 4 × 5 m block under tensile loading (mode I) is compared with this XFEM for all four materials. The stress intensity factors fall within 10 % of the analytical solution.

4 Results and Discussion

4.1 Asperity Scale

In the following results, normal loads applied are normalized to the critical load required to cause yielding inception for a Hertzian contact [35], i.e., for a given applied normal load, P, the normalized normal load, P^*, is given as $P^* = \frac{P}{P_c}$. The tangential load, Q, is normalized to the normal load applied, P, and the tangential displacement is normalized to the interference after the normal loading, ω_o. The simulations are carried out for dimensionless normal loads, P^*, ranging from 0.1 to 30. The sliding inception is investigated for this range of P^* values as it covers both elastic as well as plastic region and encompasses most real-life scenarios and applications [51, 52]. At rough surface scale, bulk material yielding will be initiated at A_nY. The critical load for yielding inception for a spherical asperity is $\sim 1.1\, A_rY$, where A_r is the real contact area [42]. The real area of contact is few percent (typically 2–3 %) of the nominal contact area [53–57]. Thus, taking the ratio of the two loads and substituting A_r in terms of A_n, we estimate the P^* value of ~ 30. The ratio of A_n/A_r will determine the extent of load carried by an asperity. If the entire load applied at the rough surface is carried by a few sharper protruding asperities, then the dimensionless normal load, P^*, will be higher than 30 [6, 36, 58]. We account for the higher dimensionless normal loads by integrating theoretical predictions with our FEM results (see discussion for Fig. 8). In addition, the energy dissipation distribution at a given loading instance is given in terms of percentages among plasticity, cracks and interfacial slip, that is, the right-hand side of Eq. (6) equals 100 %. Bar plots are used to present the energy dissipation partitioning.

4.1.1 Effect of Cracks

The first set of results presented covers the fully adhered local contact condition for material A and includes the effects of crack propagation, i.e., the XFEM module is turned on. Figure 3 shows the results for dimensionless tangential load, Q/P, versus dimensionless tangential displacement, u_x/ω_o, for $P^* = 0.1$; the corresponding % energy dissipation at different stages of tangential loading and the snapshots of evolution of the crack surface in XFEM at these stages. As observed from Fig. 3a, the curve starts with a straight line; however, as the tangential load increases, the instantaneous tangential stiffness gradually decreases and ultimately reaches zero at the onset of sliding. To reduce the computation times, sliding inception is said to occur when the tangential stiffness is below 10 % of its initial stiffness. The normalized tangential force, Q/P at

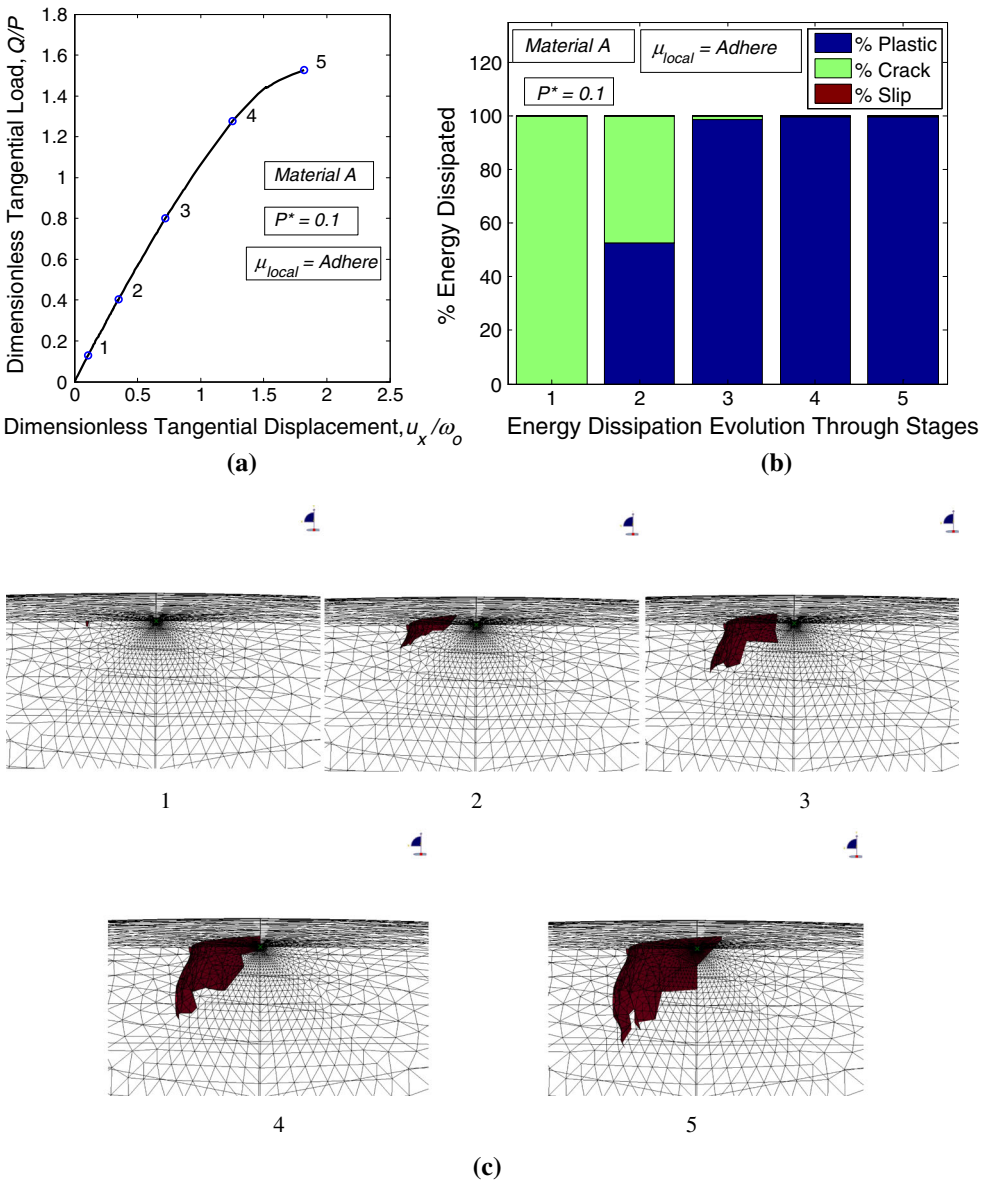

Fig. 3 **a** Dimensionless tangential load, Q/P, versus dimensionless tangential displacement, u_x/ω_o, for dimensionless normal load $P^* = 0.1$ for material A with five different points marking the evolving tangential stiffness, **b** corresponding plot for % energy dissipated at each of the five intervals and **c** snapshots of evolution of crack through different stages for dimensionless normal load $P^* = 0.1$ for material A

the onset of sliding is considered as the global static coefficient of friction, i.e., it is the average friction coefficient at the interface. Energy dissipation evolution throughout the tangential loading provides valuable insights into the relative contribution of each mechanism on the tangential compliance.

As evident from Fig. 3b, initially when the tangential loading is applied, the energy is dissipated by crack only. The crack initiates in the tensile zone at the specified limiting maximum principal stress and starts propagating at stage 1 as seen in the snapshot of crack in Fig. 3c. As the crack initiates, it is also surrounded by the plastic zone since the cohesive zone approach is used for modeling the crack. However, the energy dissipated by this plasticity near the crack tip is negligible compared with the energy loss due to crack surface formation. As expected, there is also no frictional loss due to interfacial slip, since the contact is fully adhered and does not allow any relative motion between contacting surfaces. The crack continues to propagate along the periphery of the principal stress contours. As the tangential load increases, plasticity comes into effect and the energy is dissipated by both the plasticity and crack. With increasing tangential load, the compressive zone below the contact gradually transitions to tensile zone and the crack starts to penetrate deeper. Finally, the maximum crack propagation is observed at step 5 at the inception of sliding. However, at this time, the material at the contact has substantially yielded due to increasing shear loading and it overshadows the contribution of the crack. As a result, plasticity dominates the

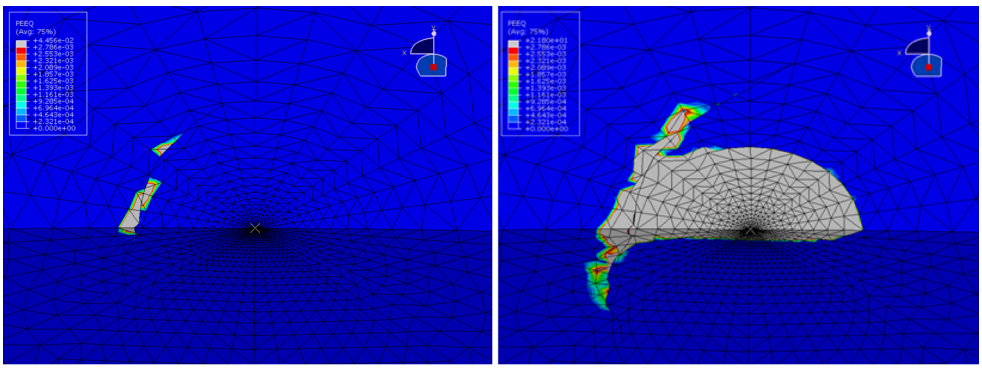

(a) (b)

Fig. 4 Plastic equivalent strains for dimensionless normal load $P^* = 0.1$ for material A **a** for stage 2 in Fig. 3c and **b** for stage 5 in Fig. 3c

energy dissipation at sliding inception. This can also be verified by studying the plastic equivalent strains at the contact interface.

Figure 4 shows the plastic equivalent strains for dimensionless normal load, $P^* = 0.1$ and material A at stage 2 and at stage 5 described in Fig. 3c. Stage 2 corresponds to the initial phase of tangential loading, whereas stage 5 corresponds to the maximum tangential load at sliding inception. Cohesive zone approach is used for modeling crack, and there is some accompanying plasticity with crack propagation, which makes it difficult to distinguish between the plasticity associated with material yielding due to loading and plasticity associated with crack propagation. At stage 2, the % plasticity in the energy dissipation plot (see Fig. 3b) is possibly associated with crack propagation, as seen from Fig. 4a, whereas at stage 5, the % plasticity in the energy dissipation plot (see Fig. 3b) is dominated by material yielding at the contact due to the applied tangential load (see Fig. 4b). This demonstrates that the energy dissipated by plasticity is higher than the energy dissipated by crack at sliding inception; thus, the presence of crack does not significantly alter the static friction coefficient value.

With increasing dimensionless normal load ($P^* > 1$), the effect of crack diminishes even further (not shown). The extent of plastic deformations increases with increasing P^*, leading to a more uniform stress field, which in turn prevents extensive crack propagation. It should be noted that the fracture toughness value used for the simulation corresponding to the material A (see Table 1) was the least among the values listed. Similar results were obtained for the remaining set of materials indicating that static friction coefficients are independent of fracture toughness under our definition of the onset of sliding. These observations lead to an early remark, the minute flaws or underlying cracks at the asperity scale do not substantially alter the energy dissipation and friction coefficient. Based on this remark, the XFEM module is turned off for subsequent simulations, and thus, only the relative importance of interfacial slip and plasticity is investigated further.

4.1.2 Effect of Local Friction (Interfacial Strength)

To investigate the effects of interfacial slip on sliding inception, Coulomb friction coefficient values 0.2 through 1 are assigned to the contact and simulations are carried out for the same set of dimensionless normal loads, P^*.

Figure 5 shows the results for dimensionless tangential load, Q/P, versus dimensionless tangential displacement, u_x/ω_o, for three different P^* values for friction coefficient 0.2 for material A, and the corresponding % energy dissipation plot at the sliding inception for each P^* value. In all loading cases, sliding inception occurs when the ratio Q/P reaches a value of 0.2. In other words, the local and global friction coefficients coincide, verifying load-independent Coulomb friction and Cattaneo–Mindlin's interfacial slip approach. The % energy dissipation plot confirms that interfacial slip is the major contributor to the inception of sliding, with little to no contribution from plasticity for lower dimensionless normal loads. It should be noted that for normal loads that cause material yielding ($P^* > 1$), the energy dissipated due to plasticity in normal loading is subtracted to give the energy dissipated by plasticity during tangential loading only. This helps provide a better comparison between different mechanisms during tangential loading alone. At high dimensionless normal loads ($P^* = 10$), the material has yielded significantly and both plasticity and interfacial slip play role. However, interfacial slip still dominates, and the global friction coefficient is not influenced much by plasticity.

To see the effect of decreasing interfacial slip, local friction coefficient is set to 1, and simulations are carried out for the same set of dimensionless normal load, P^*. Figure 6 shows the results for dimensionless tangential load, Q/P, versus dimensionless tangential displacement, u_x/ω_o, for three different P^* values for material A. As observed from the figure for $P^* = 0.1$, sliding inception occurs when the ratio Q/P reaches the assigned value of local coefficient of friction 1. However, dimensionless normal load $P^* = 1$ and, $P^* = 10$ show an interesting

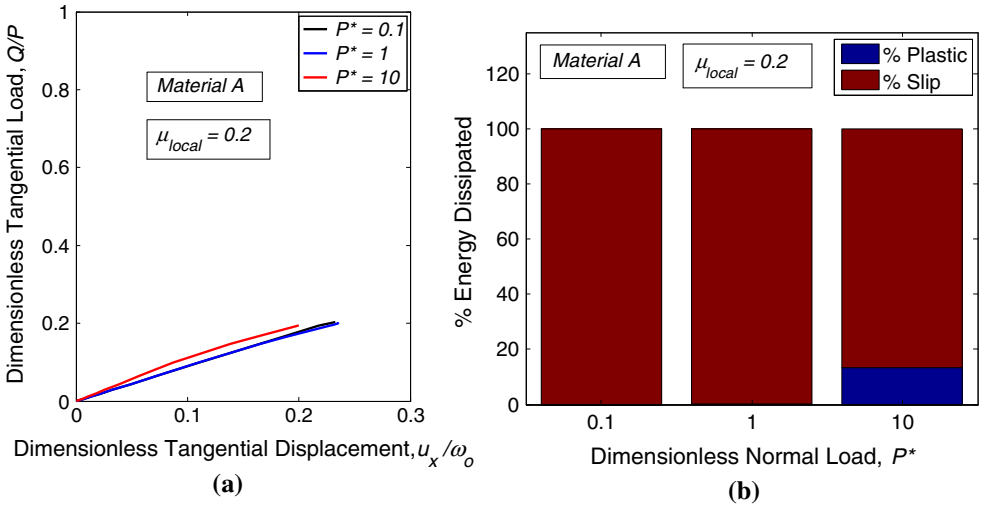

Fig. 5 **a** Dimensionless tangential load, Q/P, versus dimensionless tangential displacement, u_x/ω_o, for local friction coefficient 0.2 for material A for different dimensionless normal loads P^* and **b** corresponding plot of % energy dissipated by each mechanism (plasticity and slip) at sliding inception

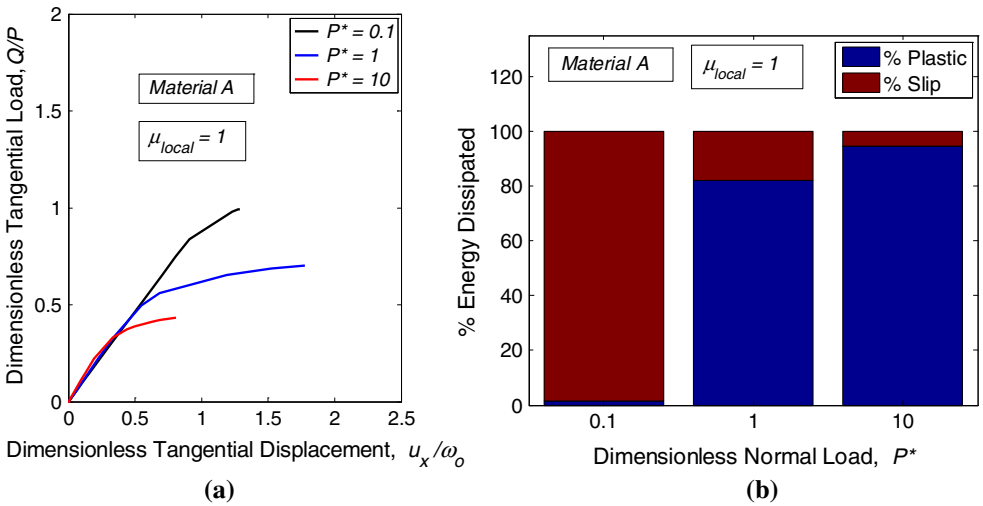

Fig. 6 **a** Dimensionless tangential load, Q/P, versus dimensionless tangential displacement, u_x/ω_o, for local friction coefficient 1 for material A for different dimensionless normal loads P^* and **b** corresponding plot of % energy dissipated by each mechanism (plasticity and slip) at sliding inception

behavior at the onset of sliding. Although the contact has been assigned a local friction coefficient of 1, sliding inception occurs below this value. The corresponding % energy dissipation plot gives more insight into the behavior of the contact at higher dimensionless normal loads. As Fig. 6b shows, frictional loss is the major contributing mechanism for sliding inception at the low dimensionless normal load, $P^* = 0.1$. The energy dissipated by interfacial slip, however, decreases with increasing dimensionless normal load. For $P^* = 1$ and 10, the contribution comes from both plasticity and interfacial slip, but plasticity starts to dominate interfacial slip. Thus, plasticity weakens the contact and lowers the global coefficient of friction below the locally assigned value at higher normal loads.

Re-emphasizing the definition of friction coefficient in this paper, the contact conditions assigned (fully adhered, 0.2 to 1 Coulomb friction coefficient) are considered as the local friction coefficients, i.e., it is the local interaction between each node at the contact and signifies adhesion shear strength of the interface. The global static coefficient of friction is the value at which the onset of sliding is said to occur when the instantaneous tangential stiffness in the dimensionless tangential load (Q/P) versus dimensionless tangential displacement (u_x/ω_o) plot gradually diminishes below 10 % of its initial stiffness. Figure 7 presents the global static friction coefficients, μ_{global}, versus dimensionless normal load, P^*, for a contact with locally assigned finite friction coefficient values ranging from 0.2 to 1 and adhered local contact for material A.

As observed from figure, all the global friction coefficient curves start at the locally assigned finite friction coefficient at lower dimensionless normal load. For the lower coefficient of friction 0.2, the local and global friction coefficients are essentially equal for all loading conditions. However, for the higher finite friction coefficient values, the local and global values differ substantially at

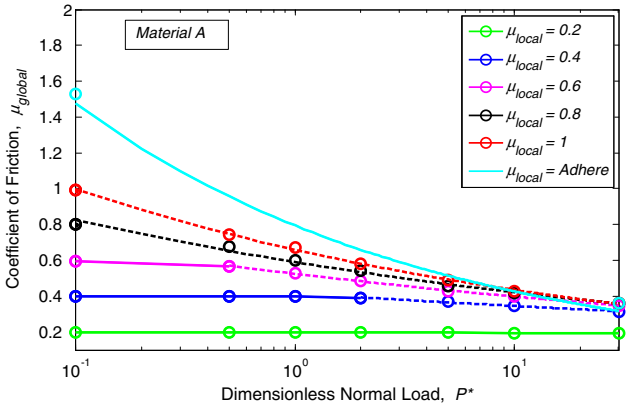

Fig. 7 Static coefficient of friction, μ_{global}, versus dimensionless normal load, P^*, for material A for different local contact conditions

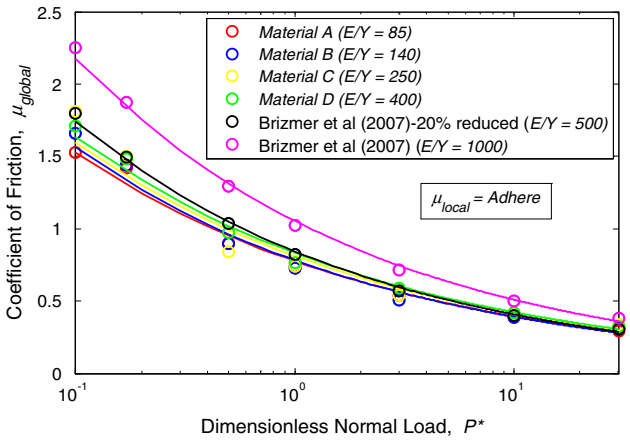

Fig. 8 Static coefficient of friction, μ_{global}, versus dimensionless normal load, P^*, for four different materials and comparison with Brizmer et al. [6] for fully adhered local contact

higher dimensionless normal loads, which is consistent with the energy distribution results suggesting the relative influence of plasticity exceeding the influence of interfacial slip at higher normal loads. As expected, the locally adhered contact displays the maximum strength at the interface with higher global coefficient of friction values, since plasticity is the only weakening mechanism with no influence of contact slip. The global curve for local coefficient of friction 0.2 which is largely immune to the effects of plasticity continues to exhibit the assigned local strength at the contact interface. The results presented are for material A with E/Y ratio 85, and the influence of E/Y on the interfacial strength is discussed in the following section.

4.1.3 Effect of E/Y

To illustrate the effect of E/Y, locally adhered contact condition is considered initially as only plasticity influences the global coefficient of friction. Figure 8 shows the global static coefficient of friction, μ_{global}, versus dimensionless normal load, P^*, for a fully adhered contact for four different materials with varying E/Y ratios. The figure also includes the results from the elastic–plastic regular FEM documented in Brizmer et al. [6] for comparison.

The materials studied here have E/Y values ranging from 85 to 400. It should be noted that the static friction coefficient values shown in Brizmer et al. [6] are reduced by 20 % in order to account for the difference in the E/Y ratio. Approximately, 15–20 % drop in the static coefficient of friction is documented in Brizmer et al. [6] when the E/Y ratio is reduced from 1,000 to 500. This suggests E/Y ratio might play an important role in sliding inception, and our results corroborate this observation with similar reduction in static coefficient of friction observed with decreasing E/Y ratio. The curve fit to the coefficient of friction data shown in Fig. 8 for all E/Y ratios takes the form of a power law given as,

$$\mu_{\text{global}} = \alpha(P^*)^{\lambda} \tag{23}$$

The coefficients α and λ for each material and Brizmer et al. [6] are summarized in Table 2. The coefficient α varies linearly with respect to the E/Y ratio on a log-linear plot. The curve fit for α takes the following form,

$$\alpha = 0.7416e^{0.0003\frac{E}{Y}} \text{ and } \lambda \approx -0.3 \quad \text{(see Table 2)}$$

Choosing the power law fit to the friction coefficient data gives mathematical simplicity and enables closed-form solutions at the rough surface scale (for uniform height distribution, see Sect. 4.2.4). However, for very high loads, the model predicts global coefficient of friction asymptotically approaching zero. At very high normal loads, the theoretical prediction for static coefficient of friction for metallic contacts is the ratio of shear strength, τ, to the hardness, H, of the metal. The shear strengths of common metals are approximately half of their yield strengths, Y, and hardness can be approximated as, $H = 3Y$, giving a ratio of ~ 0.167 [3, 59]. Thus, Eq. (23) is modified to incorporate a realistic friction coefficient at extremely high loads and is rewritten as,

Table 2 Coefficients α and λ for adhered contact for four E/Y ratios and Brizmer et al. [6]

Material	E/Y	α	λ
A	85	0.776	−0.2942
B	140	0.7705	−0.3172
C	250	0.8112	−0.294
D	400	0.8404	−0.2993
Brizmer et al. 20 % reduced	500	0.843	−0.3154
Brizmer et al.	1,000	1.0537	−0.3154

$$\mu_{\text{global}} = \max\left(0.167, \alpha(P^*)^{\lambda}\right) \tag{24}$$

The exponent λ for each material is nearly constant, approximately around -0.3 (see Table 2). This can be explained using known adhesive friction formulation. Assuming a constant shear strength at the contact interface, friction force at sliding inception then would simply be the product of that shear strength and the contact area, i.e., $Q \sim a^2$. The shear strengths at the interface for each *E/Y* ratio are computed by the FEM as 0.5–0.6 times the yield strength of the material. For all four ratios, only slight variation in shear strength is observed (<10 %) for the range of normal loads studied. Neglecting the effects of junction growth upon tangential loading, Hertzian theory suggests that the square of contact radius scales with the normal load as $a^2 \sim P^{2/3}$. Our FEM results for fully adhered contact exhibit marginally different relation as $a^2 \sim P^{2.1/3}$. Therefore, $Q \sim P^{2.1/3}$, and $\mu = Q/P \sim P^{-0.3}$. This is remarkably close to the observed exponents. Based on the adhesive frictional formulation and dimensionless analysis (see "Appendix"), it can be shown that increasing the yield strength and decreasing the Young's modulus increase the static coefficient of friction. A larger *Y/E* ratio would imply a larger recoverable elastic strain, suggesting smaller energy dissipation and lesser weakening of the contact interface, giving a higher static coefficient of friction for locally adhered contact. To investigate the effect of *E/Y* on global static coefficient of friction for contact conditions with finite local interfacial strength, simulations were carried out for the remaining materials for contact conditions with local Coulomb friction 0.2–1 (similar to Sect. 4.1.2).

The results for global static coefficient of friction, μ_{global}, versus dimensionless normal load, *P**, for different materials for finite local contact friction are shown in Fig. 9. As observed from figure, for higher local contact friction, the global coefficient of friction showed minimal dependency on the *E/Y* ratio for the range of values considered in this study. For lower local contact friction, the global coefficient of friction was independent of the *E/Y* ratio. The dotted lines in Fig. 9 (and in Fig. 7) are in form of a power law. The coefficient α shows a power law dependency on the local interfacial strength, and no dependency on the *E/Y* ratio, whereas exponent λ shows linear relation with the local interfacial strength and minimal dependency on *E/Y* ratio. Thus, the equation for global coefficient of friction can now be given as,

$$\mu_{\text{global}} = \min\left(\mu_{\text{local}}, \max\left(0.167, \alpha(P^*)^{\lambda}\right)\right) \tag{25}$$

where

$$\alpha = 0.6931\mu_{\text{local}}^{0.7153}$$

$$\lambda = -0.223\mu_{\text{local}} + \left(-0.00002\frac{E}{Y} + 0.0261\right)$$

For finite local friction contact, the *E/Y* term in λ in Eq. (25) can be neglected.

Figure 10 shows the static friction coefficient, μ_{global}, versus the dimensionless normal load, *P**, for a fully adhered local contact, and comparisons with the experimental data from Ovcharenko et al. [60] and predictions from Brizmer et al. [6].

The experimental results were obtained by performing static friction tests on a copper ball of 5 mm diameter and *E/Y* ratio of 400 under adhered local conditions [60]. The present model gives an improvement on the model in Ref. [6] and compares better with the experimental data as it incorporates the *E/Y* dependency. If locally adhered

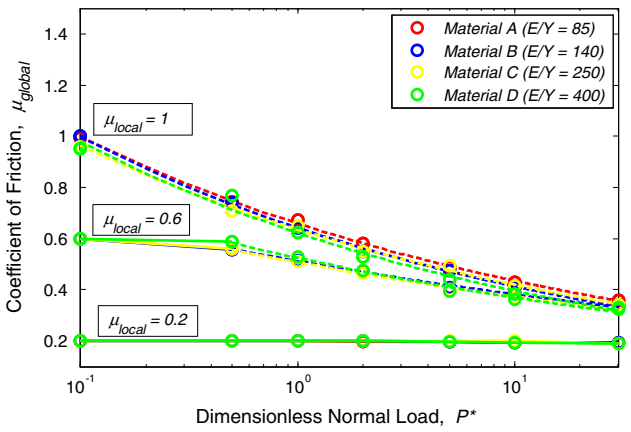

Fig. 9 Static coefficient of friction, μ_{global}, versus dimensionless normal load, *P**, for different materials for different local contact friction coefficient 1, 0.6 and 0.2

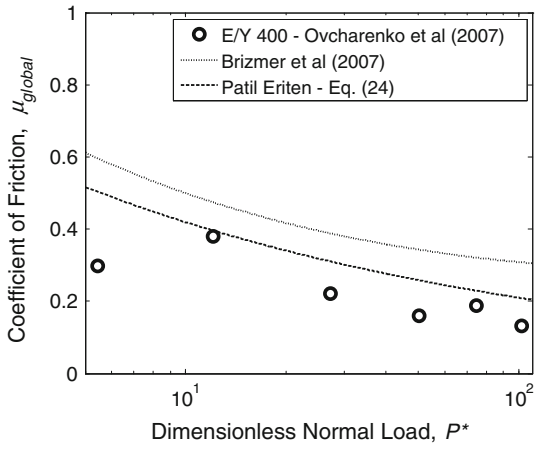

Fig. 10 Static coefficient of friction, μ_{global} versus dimensionless normal load, *P** for fully adhered local contact and comparisons with Brizmer et al. [6] and experimental data from Ovcharenko et al. [60]

conditions are violated in the experiments, then including the finite local friction would further improve the correlation with the experimental data.

4.2 Rough Surface Scale

The friction coefficient in Eq. (21) takes the closed-form expression given in Eq. (28) for adhered local friction and Eq. (29) for finite local friction. The total dimensionless maximum tangential load, $Q'_{\max}$ carried by the rigid flat can now be given by Eq. (31) (see "Appendix" for details). The static friction coefficient at rough surface is the ratio of maximum tangential load carried by the rigid flat at sliding inception over the normal load supported by the flat,

$$\bar{\mu} = \frac{Q'_{max}}{P'} \tag{26}$$

The plasticity index, ψ is varied from 0.2 to 8, as it spans both the elastic and plastic contact regimes, and the surface roughness parameter, β is set to 0.04 as in Cohen et al. [21]. The dimensionless normal load, $P' = P_{\text{flat}}/A_{\text{n}}Y$ is varied between a lower limit of 0.0001 and an upper limit of 0.3. The upper bound is set to 0.3 to be within the limits encountered in practical applications [61, 62]. The asperity distribution is assumed to be Gaussian (revisited in Sect. 4.2.4), with the dimensionless asperity height variation z^* between -3 and $+3$. The static friction coefficient [Eq. (26)] can now be plotted against the dimensionless normal load (Eq. (30)] for a varying combination of parameters, such as plasticity index, E/Y ratio and local friction coefficient, giving valuable insights into the strength of the contact interface.

Figure 11 shows the static friction coefficient at rough surface, $\bar{\mu}$, versus the dimensionless normal load, P', for material A for different plasticity indices and local interfacial strengths. As observed from the figure, the coefficient of friction, $\bar{\mu}$, decreases with increasing plasticity index, ψ. At higher plasticity index, the asperities are not able to sustain larger tangential loads as the interface has substantial amount of plasticity. The effect of plasticity index is more prominent for higher local friction coefficient (see Fig. 11a, b) and less so with decreasing local friction coefficient (see Fig. 11d). This is because of the increase in interfacial slip with decreasing local friction coefficient. It can also be observed that for the same plasticity index, the coefficient of friction decreases with increasing dimensionless normal load. A similar behavior was observed at asperity scale (presented in the previous subsection), increasing normal load increases the material yielding and plasticity and thereby weakens the contact interface. However, for higher plasticity index, the static friction coefficient is nearly constant. Constant static friction coefficient independent of normal load at higher plasticity index was observed by Gao et al. [63] for thin potassium chloride film deposited on different substrates. For lower plasticity index, static friction coefficients were load-dependent and decreased with increasing normal load [63].

The parameters such as local contact friction, plasticity index, E/Y ratio and surface height distribution are non-deterministic as they vary with time and/or with running-in of the surface, thus changing the contact conditions. As it is extremely difficult to predict and control these parameters, the stochastic effects due to surface roughness and material property uncertainties and their influence on the static coefficient of friction are discussed in the following sections.

4.2.1 Effect of Local Friction (Interfacial Strength)

Re-emphasizing, the local friction coefficient values in our study represent adhesion shear strength of the interface. Figure 12 shows the significance of the local interfacial strength; the coefficient of friction, $\bar{\mu}$ is normalized with respect to the coefficient of friction, $\bar{\mu}$, for an adhered local contact, and is plotted against the dimensionless normal load, P', for different local contact conditions for plasticity index, $\psi = 0.5$ and material A.

Assuming the contact to be fully adhered can lead to erroneous results especially for lower dimensionless normal loads. Mechanisms other than plasticity such as interfacial slip will have a role in sliding inception. Fully adhered assumption will be invalid if the surfaces are contaminated, as well as in the presence of humidity and surface films. Ibrahim Dickey et al. [64] claim the presence of oxide film formation on a tin surface invalidates the perfect adhesion between the surfaces. Their experiments show the static friction coefficients for tin surface with an oxide layer to be approximately lower by 0.25 as compared to fully adhered contact. Hence, it is essential to take local interfacial strength into consideration. However, it is noteworthy to discuss the difficulty in defining local friction coefficients at a particular contact problem especially since it is a system-dependent property. At nanometer scale, Zappone et al. [65] observed the static friction coefficient of ~ 2 for cross-linked stiff polymers with RMS roughness value 0.5 nm; however, for RMS roughness 7.1 nm, the static friction coefficient decreased to 0.74. In ideal situations, experiments and/or simulations at atomistic scales could yield the interfacial strength in a given contact configuration. Alternatively, quasi-static fretting tests covering gross-sliding regime at nano-/micro-length scales could retrieve valuable information about the local friction coefficient of a macroscale contact application. The authors are currently working on it with various materials.

The above results were for low plasticity index, i.e., predominantly elastic contact. Next, we discuss the effect of plasticity index, ψ.

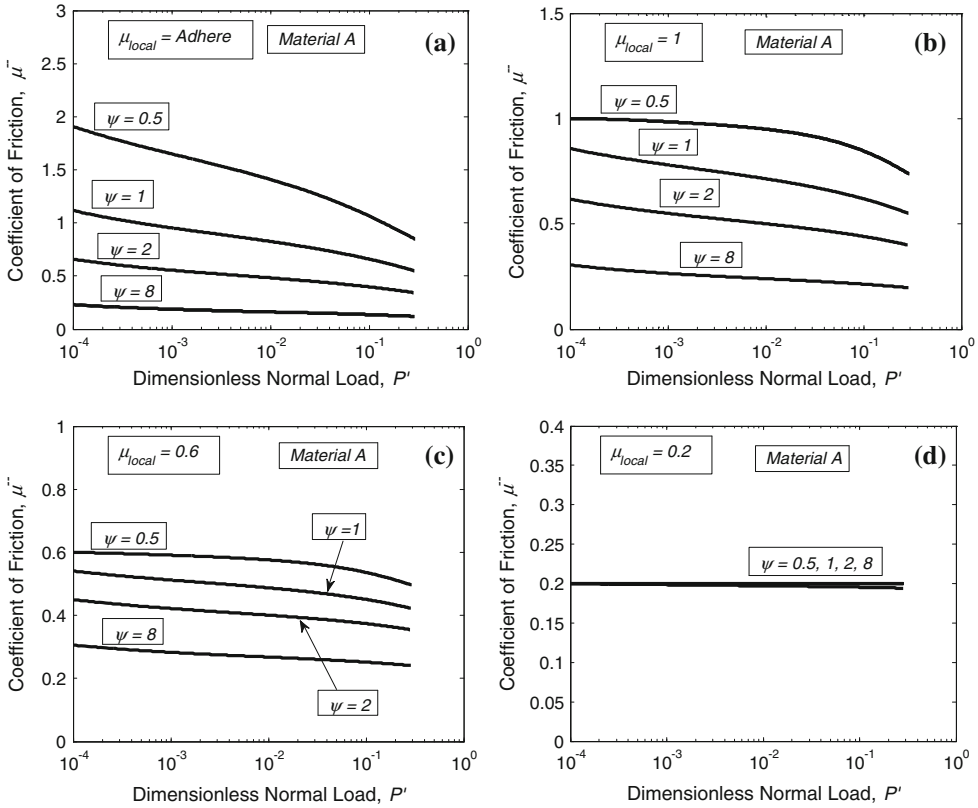

Fig. 11 Static coefficient of friction, $\bar{\mu}$, versus dimensionless normal load, P', for material A and for different plasticity indices for **a** adhere local contact, **b** local contact friction coefficient 1, **c** local contact friction coefficient 0.6 and **d** local contact friction coefficient 0.2

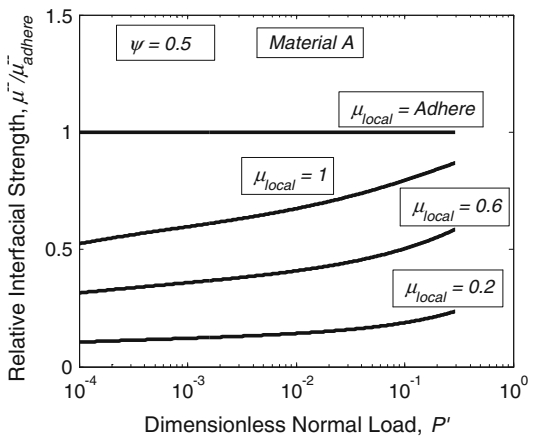

Fig. 12 Static coefficient of friction, $\bar{\mu}$ normalized with respect to static coefficient of friction, $\bar{\mu}$ with adhere local contact versus dimensionless normal load, P', for material A and plasticity index $\psi = 0.5$ for different local contact conditions

4.2.2 *Effect of Plasticity Index, ψ*

The coefficient of friction, $\bar{\mu}$ is normalized with respect to the coefficient of friction, $\bar{\mu}$ for plasticity index $\psi = 0.2$ (fully elastic contact), and is plotted against the plasticity index, ψ for different local contact conditions for dimensionless normal load, $P' = 0.1$ and material A in Fig. 13. A rougher surface, sharper asperities, and softer material will all increase the plasticity index [see Eq. (19)]. Plasticity index can change depending upon the running-in of the surface. The running-in process generates smooth surfaces with a lower plasticity index due to flattening of the peaks, and work-hardening effect due to the repeated deformation of asperities [66]. The variation in plasticity index occurs in practical applications such as running-in of bearings [67] and needs to be taken into account for the correct estimation of static friction. The experiments in Ref. [67] show the plasticity index value drop from 1.4 to 0.7 after 25 h of running-in period for roller bearings; this approximately amounts to a 50 % increase in static friction coefficient under locally adhered contact (see Fig. 13). A more dramatic change was observed in Ref. [64] where the formation of oxide layer on tin surfaces was found to reduce the plasticity indices from 15 to 2–8. In calculation of these indices, the authors in Ref. [64] assumed the surface roughness to be constant before and after oxidation, and incorporated only the change in the material properties due to oxidation. This assumption will be valid only if the thickness of the oxide layer is uniform throughout the nominal contact area. Their friction experiments after oxidation show that for a dimensionless normal load, $P' \sim 0.001$, the static friction coefficient is approximately 0.17. For this contact, our model predicts a static friction coefficient of $\sim$0.21 under fully adhered contact

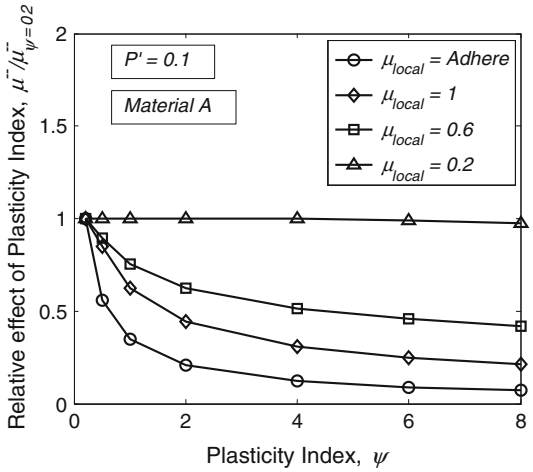

Fig. 13 Static coefficient of friction, $\bar{\mu}$ normalized with respect to static coefficient of friction, $\bar{\mu}$ at plasticity index, $\psi = 0.2$ versus plasticity index ψ for material A and dimensionless normal load, $P' = 0.1$ for different local contact conditions

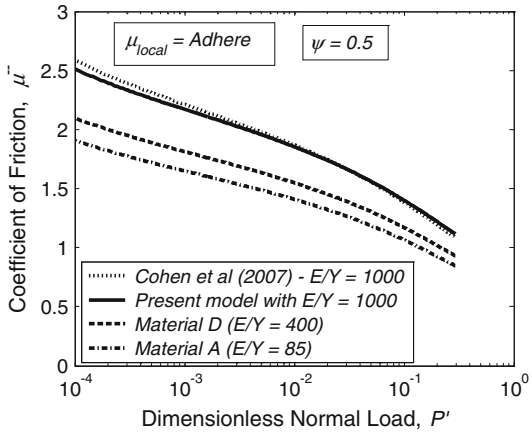

Fig. 14 Static coefficient of friction, $\bar{\mu}$, versus dimensionless normal load, P', for plasticity index, $\psi = 0.5$ and adhere local contact for different E/Y ratios and comparison with Cohen et al. [21]

conditions. If the oxide layer prevents full stick conditions, our model would predict even lower values for friction coefficient, down to the theoretical limit of 0.167 [Eq. (22)], yielding a range of friction coefficient values reasonably close to the experimental observations.

4.2.3 Effect of E/Y

Figure 14 shows the static coefficient of friction, $\bar{\mu}$, versus dimensionless normal load, P', for plasticity index, $\psi = 0.5$ and adhere to local contact for different E/Y ratios and comparison with Cohen et al. [21]. The normalization parameters used during normal loading at the asperity scale in this paper are based on Hertzian frictionless contact, whereas the normalization parameters in Cohen et al. [21] are based on fully adhered contact. To ensure a better comparison, the results from Cohen et al. [21] shown in Fig. 14 are normalized with respect to Hertzian frictionless contact. As observed from the figure, our results match well with Cohen et al. [21] for E/Y ratio of 1,000, the ratio used in their study. However, as the E/Y ratio decreases, so does the static coefficient of friction: consistent with the previous observations at the asperity scale. For finite local friction coefficients, minimal dependency on E/Y ratio was observed at the asperity scale, and similar behavior prevails at rough surface scale as interfacial slip is expected to be more influential than plasticity on the inception of sliding.

In practice, the yield strength for the same material can change even during the surface treatment process; for instance, the yield strength of the laser-peened steel increased by a factor of two compared with the yield strength of the virgin surface [68]. At lower dimensionless normal loads and locally adhered contact with plasticity index, $\psi = 0.5$, this increase in yield strength for steel will amount to approximately 12 % variation in the static friction coefficient and, hence, should be always accounted for materials-related uncertainty in frictional response.

4.2.4 Surface Height Distribution Comparison

The results at the rough surface scale presented thus far are based on symmetric normal distribution ($\sigma_{sk} = 0$) for the surface heights. The running-in process can produce highly asymmetric asperity height distribution with high skewness and kurtosis values, which can influence the static coefficient of friction [24, 69, 70]. Lee et al. [24] show increasing static friction coefficient with running-in; under dry conditions, the coefficient of friction for steel increased by a factor of 2 and by a factor of 5 after 10 min and 10^4 min of running-in period, respectively. The running-in process tends to create surfaces with negative skewness values [24]. Yu et al. [69] show strong dependency of static friction coefficient on the skewness value: negative skewness increasing the static coefficient of friction. Common manufacturing techniques such as grinding, honing, milling and laser cutting produce surfaces with skewness values approximately around -1 [71]. To demonstrate the dependency of static friction coefficient on surface height distributions, an example case of Weibull distribution with skewness value, $\sigma_{sk} = -1$, is compared with the normal distribution. Furthermore, to show the effects of kurtosis (σ_{ku}) and enable analytical solutions, a comparison for triangular distribution and uniform distribution for surface heights is also presented.

The four asperity height distributions are shown in Fig. 15. Each asperity height distribution has the same

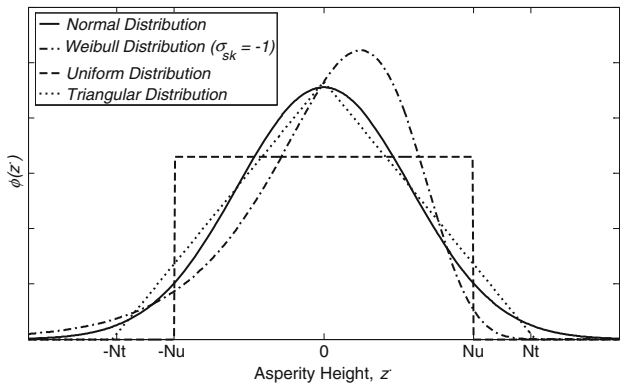

Fig. 15 Different asperity height distributions

Table 3 Skewness and kurtosis values for different asperity height distributions

Distribution	Skewness (σ_{sk})	Kurtosis (σ_{ku})
Normal	0	3
Uniform	0	1.8
Triangular	0	2.4
Weibull [26]	−1	~4.7

standard deviation, σ_s, and is normalized with respect to the standard deviation of the surface height, σ. Nu and Nt in Fig. 15 are the limits for asperity height for uniform distribution and triangular distribution, respectively, to obtain the same standard deviation, σ_s. The details of the probability density function for each asperity height distribution are given in the "Appendix." Table 3 shows the skewness and kurtosis values for the four distributions. Substituting Eqs. (32)–(34) into Eqs. (30) and (31), and subsequently into Eq. (26), the coefficient of friction, $\bar{\mu}$ can be obtained for uniform distribution, triangular distribution and Weibull distribution, respectively.

Figure 16 shows the static friction coefficient, $\bar{\mu}$, versus the dimensionless normal load, P', for material A for plasticity indices $\psi = 0.5$ and $\psi = 8$ and different local friction coefficients, for the four surface height distributions.

As observed from Fig. 15a, at higher dimensionless normal loads, the difference between the coefficient of friction for the four distributions is negligible. This is because the asperities are deformed significantly and the height distribution becomes insignificant. However, for lower dimensionless normal loads and plasticity index, $\psi = 0.5$, kurtosis influences the static coefficient of friction

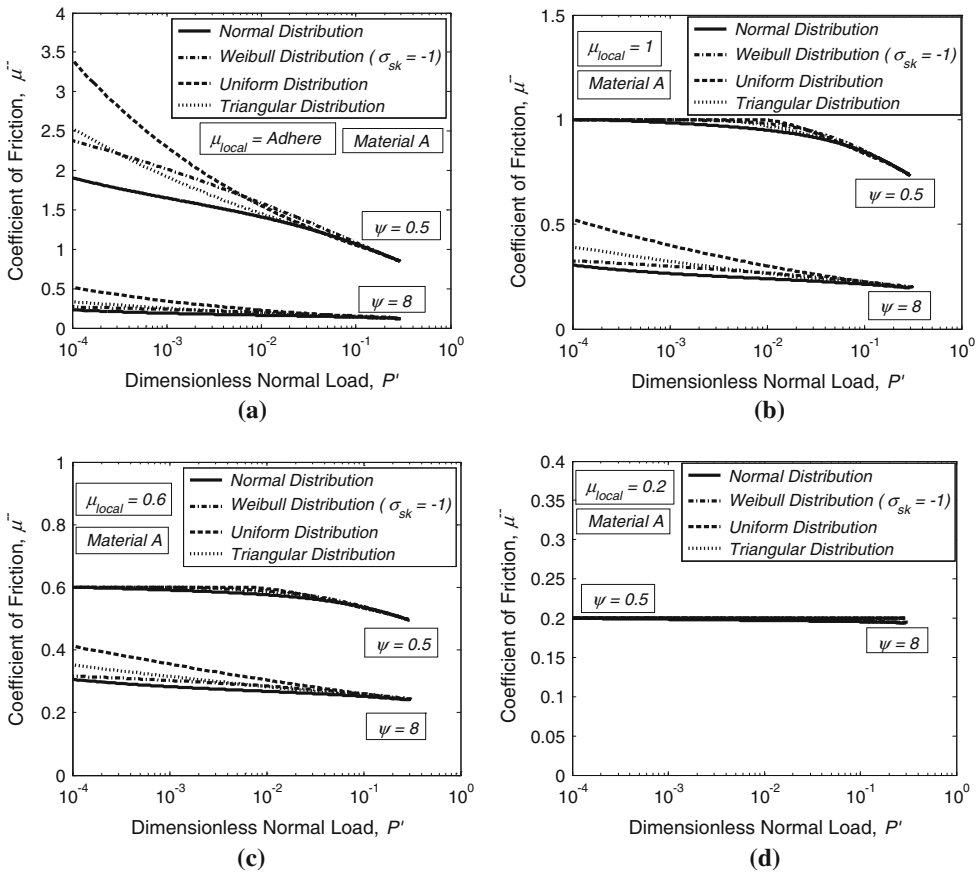

Fig. 16 Static coefficient of friction, $\bar{\mu}$, versus dimensionless normal load, P', for different asperity height distributions for material A and plasticity index $\psi = 0.5$, and 8 for **a** adhere local contact, **b** local contact friction coefficient 1, **c** local contact friction coefficient 0.6 and **d** local contact friction coefficient 0.2

significantly; for uniform distribution ($\sigma_{ku} = 1.8$), the static friction coefficient is around 80 % greater compared with the normal distribution ($\sigma_{ku} = 3$). For the same normal load, uniform distribution will have more asperities in contact compared with normal distribution. As the normal load is being supported by more asperities, the contact will be damaged to a lesser extent and larger tangential load will be required to cause sliding inception. Skewness coupled with kurtosis also effects the static friction coefficient; Weibull distribution ($\sigma_{sk} = -1$, $\sigma_{ku} = 4.7$) shows approximately 30 % increase in static coefficient of friction compared with normal distribution for adhered local contact at lower dimensionless normal load and plasticity index, $\psi = 0.5$. For finite local friction coefficient, all four distributions converge to the assigned local value at lower dimensionless normal load and plasticity index, $\psi = 0.5$. At higher normal load, similar behavior to the adhered local contact is observed. With decreasing local friction coefficient, the variation in the static friction coefficient for the four distributions disappears, as the local interfacial slip governs the sliding inception.

Choosing uniform distribution will enable closed-form solutions for the integrals in Eqs. (30) and (31). Plugging these equations in Eq (26), an analytical expression can be derived for the coefficient of friction (see "Appendix"). The static coefficient of friction is a function of dimensionless normal load, P', plasticity index, ψ, and surface roughness parameter, β, ratio of standard deviation of surface and asperity heights, σ/σ_s, Poisson's ratio, ν, E/Y ratio and the local interfacial strength, μ_{local}. All the parameters except for the local friction coefficient are readily available (material properties) or can be easily measured (roughness parameters). Once a reliable measure for the local friction coefficients is obtained, Eq. (35) can be used to determine the static friction coefficient at different loading conditions for uniform surface height distributions.

5 Conclusion

Finite element simulations are carried out for a rigid flat on a deformable sphere under combined normal and tangential loading at the asperity scale. The sphere is subjected to dimensionless normal load, P^*, ranging from 0.1 to 30, followed by a monotonic tangential loading until the onset of sliding occurs. The onset of sliding is modeled after the complete loss of tangential stiffness due to interplay among three major mechanisms, namely interfacial slip, plasticity and crack propagation. It is observed that cracks do not influence the onset of sliding significantly. A discussion on the material properties influencing the friction coefficients suggests that increasing ratio of yield strength to Young's modulus, a measure of recoverable strain in a material increases the friction coefficient in a fully adhered contact. For the contact with the coefficient of local friction 0.6 and higher, it is observed that at higher dimensionless normal loads, weakening of contact is controlled by the interplay between plasticity and interfacial slip, eventually lowering the global friction coefficient below the assigned local value.

The single asperity results are incorporated in a statistical model for nominally flat contacting rough surfaces under combined normal and tangential loading to investigate the stochastic effects due to the surface roughness and material property uncertainties. The static friction coefficient shows strong dependency on parameters, such as local interfacial strength, plasticity index, material properties and surface height distributions. It is very difficult to predict and control these parameters due to running-in of the surface and chemical processes, such as oxide film formations. Consequently, a range of static friction coefficient values are given which can be used as bounds to account for the uncertainties in roughness and material property. A comparison of the present results with those of a previously published elastic–plastic model shows good correlation for static coefficient of friction under locally fully adhered contact. Additionally, the present model gives dependency on finite local interfacial strength. The authors are currently developing set of experiments to measure a representative local interfacial strength. Furthermore, in situ imaging of the contact and using techniques such as digital image correlation (DIC) at nanoscale can give valuable insights into behavior of the interface and reveal any interfacial slip and/or material flow. Once a reliable measure of local interfacial strength is obtained, the effectiveness of our model will be verified with the experimental results for static friction coefficient at the rough surface scale.

Appendix 1

Dimensionless Analysis for Dependence of μ_{global} on E/Y for Adhered Local Contact

A dimensional analysis is needed for better understanding of the effects of the parameters as Young's Modulus, E, yield strength, Y and the radius of the sphere, R on the global static coefficient of friction for an adhered local contact. When Eq. (15) is substituted in Eq. (23), and exponential term is expanded for $0.0003E/Y << 1$, leading term $O(2)$;

$$\mu = 0.7416(1 + 0.0003(E/Y))\left(\frac{P}{\frac{\pi^3}{6A^3}Y\left(R(1-\nu^2)\frac{Y}{E}\right)^2}\right)^{\lambda} \tag{27}$$

Table 4 Coefficients α and λ for adhered and finite friction contact

Contact condition	P^*		ω^*	
	α	λ	α	λ
Adhered	$0.7416e^{0.0003\frac{E}{Y}}$	-0.3	$0.7511e^{0.0003\frac{E}{Y}}$	-0.425
Finite Friction	$0.6931\mu_{\text{local}}^{0.7153}$	$-0.223\mu_{\text{local}} + 0.261$	$0.6925\mu_{\text{local}}^{0.7167}$	$-0.325\mu_{\text{local}} + 0.0409$

The multiplying term $0.7416(1 + 0.0003(E/Y))$ is on the order of unity for the range of E/Y values considered in this study, implying that the static coefficient of friction scales inversely with the terms in the critical load for yielding inception. Assuming λ constant with a value of -0.3, static coefficient of friction scales with Young's modulus as, $\mu \sim E^{-2/3}$, and with yield strength as $\mu \sim Y$. Thus, increasing the yield strength and decreasing the Young's modulus increase the static coefficient of friction.

Asperity Scale Static Friction Coefficient Formulations in Terms of Interference

As the asperity scale friction coefficients are to be incorporated in the statistical model at the rough surface scale, it is convenient to express Eq. (24) in terms of interference rather than the normal load. This is achieved similarly by fitting the FEM results for static friction data against the interference, with the equation again taking the form of power law and is given as,

$$\mu_{\text{global}} = \max\left(0.167, \alpha(\omega^*)^{\lambda}\right) \tag{28}$$

where $\alpha = 0.7511e^{0.0003\frac{E}{Y}}$ and $\lambda \approx -0.425$; and the dimensionless interference $\omega^* = \omega/\omega_c$.

Similarly, Eq. (25) can be expressed in terms of interference for contact condition with finite local friction as,

$$\mu_{\text{global}} = \min\left(\mu_{\text{local}}, \max\left(0.167, \alpha(\omega^*)^{\lambda}\right)\right) \tag{29}$$

where

$$\alpha = 0.6925\mu_{\text{local}}^{0.7167}$$

$$\lambda = -0.325\mu_{\text{local}} + \left(-0.00003\frac{E}{Y} + 0.0409\right)$$

The coefficient α and exponent λ for Eqs. (24) and (25), and Eqs. (28) and (29) are summarized in Table 4.

Rough Surface Scale Load Formulations

The total dimensionless normal load carried by the rigid flat is given as,

$$P' = \frac{P_{\text{flat}}}{A_n Y} = \frac{2\pi\beta}{3K_v} \times \begin{pmatrix} \psi\left(\frac{\sigma}{\sigma_s}\right)^{0.5} \int_{d'}^{d'+\omega_c'} (z' - d')^{\frac{3}{2}} \phi'(z')\mathrm{d}z' \\ +\psi^{-2}\left(\frac{\sigma_s}{\sigma}\right) \int_{d'+\omega_c'}^{d'+6\omega_c'} \left((z' - d')\frac{\psi^2\sigma}{\sigma_s}\right)^{1.425} \phi'(z')\mathrm{d}z' \\ +\psi^{-2}\left(\frac{\sigma_s}{\sigma}\right) \int_{d'+6\omega_c'}^{d'+110\omega_c'} \left((z' - d')\frac{\psi^2\sigma}{\sigma_s}\right)^{1.263} \phi'(z')\mathrm{d}z' \end{pmatrix} \tag{30}$$

The total dimensionless maximum tangential load carried by the rigid flat is given by substituting Eqs. (12)–(14) in Eq. (21), and substituting the appropriate global friction coefficient model in Eq. (21) and finally substituting Eq. (21) in the integral of Eq. (20),

$$Q'_{\max} = \frac{Q_{\max-\text{flat}}}{A_n Y} = \frac{2\pi\beta\alpha}{3K_v} \times \begin{pmatrix} \psi\left(\frac{\sigma}{\sigma_s}\right)^{0.5} \int_{d'}^{d'+\omega_c'} (z' - d')^{\frac{3}{2}+\lambda} \left(\frac{\psi^2\sigma}{\sigma_s}\right)^{\lambda} \phi'(z')\mathrm{d}z' \\ +\psi^{-2}\left(\frac{\sigma_s}{\sigma}\right) \int_{d'+\omega_c'}^{d'+6\omega_c'} \left((z' - d')\frac{\psi^2\sigma}{\sigma_s}\right)^{1.425+\lambda} \phi'(z')\mathrm{d}z' \\ +\psi^{-2}\left(\frac{\sigma_s}{\sigma}\right) \int_{d'+6\omega_c'}^{d'+110\omega_c'} \left((z' - d')\frac{\psi^2\sigma}{\sigma_s}\right)^{1.263+\lambda} \phi'(z')\mathrm{d}z' \end{pmatrix} \tag{31}$$

where

$$\alpha = \begin{cases} 0.6925\mu_{\text{local}}^{0.7167} & \text{for local finite friction} \\ 0.7511e^{0.0003\frac{E}{Y}} & \text{for local adhere friction} \end{cases}$$

$$\lambda = \begin{cases} -0.325\mu_{\text{local}} + 0.0409 & \text{for local finite friction} \\ -0.425 & \text{for local adhere friction} \end{cases}$$

Probability Density Functions for Different Asperity Height Distributions

For uniform height distribution, the asperities are distributed uniformly between the range $-\text{Nu}\sigma_s$ to $\text{Nu}\sigma_s$, where $\text{Nu} = \sqrt{3}$ to obtain the correct standard deviation [25], and the dimensionless probability density function can be given as,

$$\phi^{\cdot}(z^{\cdot}) = \frac{\sigma}{2\sqrt{3}\sigma_s} \quad \text{for } -\sqrt{3}\sigma_s/\sigma \le z^{\cdot} \le \sqrt{3}\sigma_s/\sigma \tag{32}$$

The triangular distribution for the asperity height ranges between $-\mathrm{Nt}\sigma_s$ to $\mathrm{Nt}\sigma_s$, where $\mathrm{Nt} = \sqrt{6}$ [25]. The dimensionless probability density function takes the form,

$$\begin{aligned}\phi^{\cdot}(z^{\cdot}) &= \frac{\sigma}{\sqrt{6}\sigma_s}\left(1 - \frac{z^{\cdot}\sigma}{\sqrt{6}\sigma_s}\right) \quad \text{for } 0 \le z^{\cdot} \le \sqrt{6}\sigma_s/\sigma \\ \phi^{\cdot}(z^{\cdot}) &= \frac{\sigma}{\sqrt{6}\sigma_s}\left(1 + \frac{z^{\cdot}\sigma}{\sqrt{6}\sigma_s}\right) \quad \text{for } -\sqrt{6}\sigma_s/\sigma \le z^{\cdot} \le 0\end{aligned} \tag{33}$$

For Weibull distribution using the approach detailed in Ref. [26], and normalizing with respect to surface height standard deviation, σ, the probability density function in dimensionless form is given by,

$$\phi^{\cdot}(z^{\cdot}) = \beta_w\left(B_1 + z^{\cdot}\frac{\sigma}{\sigma_s}\sqrt{B_2 - B_1^2}\right)^{\beta_w - 1} \frac{\sigma}{\sigma_s}\sqrt{B_2 - B_1^2}\mathrm{e}^{-\left(B_1 + z^{\cdot}\frac{\sigma}{\sigma_s}\sqrt{B_2 - B_1^2}\right)^{\beta_w}} \tag{34}$$

where B_n is defined in terms of the gamma function as $B_n = \Gamma(1 - n/\beta_w)$ and β_w is the dimensionless shape parameter which can be related to the skewness value; for $\sigma_{sk} = -1$, $\beta_w = 40.7$, from the table in Ref. [26]. Also, $z^{\#} = \frac{z - \eta_w B_1}{\sigma_s} = \frac{z - \eta_w B_1}{\eta_w\sqrt{B_2 - B_1^2}}$, where η_w is the dimensional scale parameter [26]. Normalizing the asperity height, z with respect to the standard deviation of the surface height, σ, we have, $z^{\cdot} = \frac{z - \eta_w B_1}{\sigma} = \left(\frac{z - \eta_w B_1}{\eta_w\sqrt{B_2 - B_1^2}}\right)\frac{\sigma_S}{\sigma}$.

Rough Surface Static Friction Coefficient Based on Uniform Asperity Distribution

where

$$P'_{1C} = \frac{2}{15\sqrt{3}}\frac{\pi\beta}{K_v}\psi\frac{\sigma_s}{\sigma}\left(\frac{1}{\psi^2}\right)^{2.5}$$

$$P'_{2C} = \frac{2.06}{14.55\sqrt{3}}\frac{\pi\beta}{K_v}\psi^{0.85}\frac{\sigma_s}{\sigma}\left(\frac{6}{\psi^2}\right)^{2.425}$$

$$P'_{3C} = \frac{2.8}{13.578\sqrt{3}}\frac{\pi\beta}{K_v}\psi^{0.526}\frac{\sigma_s}{\sigma}\left(\frac{110}{\psi^2}\right)^{2.263}$$

and,

$$\alpha = \begin{cases} 0.6925\mu_{local}^{0.7167} & \text{for finite friction} \\ 0.7511\mathrm{e}^{0.0003\frac{E}{Y}} & \text{for adhere friction} \end{cases}$$

$$\lambda = \begin{cases} -0.325\mu_{\mathrm{local}} + 0.0409 & \text{for finite friction} \\ -0.425 & \text{for adhere friction} \end{cases}$$

Thus, the static friction coefficient at rough surface is given as,

$$\bar{\mu} = \min(\mu_{\mathrm{local}}, \max(0.167, \bar{\mu}))$$

References

1. Cattaneo, C.: Sul contatto di due corpi elastici: distribuzione locale degli sforzi. Rendiconti Dell'Accademia Naz Dei Lincei **27**, 342–348 (1938)
2. Mindlin, R.D.: Compliance of elastic bodies in contact. J. Appl. Mech. **16**, 259–268 (1949)
3. Etsion, I.: Revisiting the Cattaneo–Mindlin concept of interfacial slip in tangentially loaded compliant bodies. J. Tribol. **132**, 020801–020809 (2010)
4. Bowden, F.P., Leben, L.: The nature of sliding and the analysis of friction. Proc. R. Soc. Lond. Ser. Math. Phys. Sci. **169**, 371–391 (1939)
5. Bowden, F.P., Tabor, D.: The area of contact between stationary and between moving surfaces. Proc. R. Soc. Lond. Ser. Math. Phys. Sci. **169**, 391–413 (1939)

$$\bar{\mu} = \begin{cases} \left(\frac{5\alpha}{5 + 2\lambda}\right)\psi^{\frac{8\lambda}{5}}\left(\frac{\sigma}{\sigma_s}\right)^{\frac{2\lambda}{5}}\left(\frac{15\sqrt{3}K_v}{2\pi\beta}\right)^{\frac{2\lambda}{5}}{P_1}'^{\frac{2\lambda}{5}} & \text{for } 0 \le P'_1 \le P'_{1C} \\ \left(\frac{4.85\alpha}{4.85 + 2\lambda}\right)\psi^{1.65\lambda}\left(\frac{\sigma}{\sigma_s}\right)^{0.4175\lambda}\left(\frac{14.55\sqrt{3}K_v}{2.06\pi\beta}\right)^{\frac{\lambda}{2.425}}{P_2}'^{\frac{\lambda}{2.425}} & \text{for } P'_{1C} \le P'_2 \le P'_{2C} \\ \left(\frac{4.526\alpha}{4.526 + 2\lambda}\right)\psi^{1.7675\lambda}\left(\frac{\sigma}{\sigma_s}\right)^{0.4419\lambda}\left(\frac{13.578\sqrt{3}K_v}{2.8\pi\beta}\right)^{\frac{\lambda}{2.263}}{P_3}'^{\frac{\lambda}{2.263}} & \text{for } P'_{2C} \le P'_2 \le P'_{3C} \end{cases} \tag{35}$$

6. Brizmer, V., Kligerman, Y., Etsion, I.: Elastic–plastic spherical contact under combined normal and tangential loading in full stick. Tribol. Lett. **25**, 61–70 (2007)
7. Kogut, L., Etsion, I.: A semi-analytical solution for the sliding inception of a spherical contact. J. Tribol. **125**, 499–506 (2003)
8. Ovcharenko, A., Halperin, G., Etsion, I., Varenberg, M.: A novel test rig for in situ and real time optical measurement of the contact area evolution during pre-sliding of a spherical contact. Tribol. Lett. **23**, 55–63 (2006)
9. Zolotarevskiy, V., Kligerman, Y., Etsion, I.: The evolution of static friction for elastic-plastic spherical contact in pre-sliding. J. Tribol. **133**, 034502 (2011)
10. Ovcharenko, A., Halperin, G., Verberne, G., Etsion, I.: In situ investigation of the contact area in elastic–plastic spherical contact during loading–unloading. Tribol. Lett. **25**, 153–160 (2007)
11. Jackson, R.L., Duvvuru, R.S., Meghani, H., Mahajan, M.: An analysis of elasto–plastic sliding spherical asperity interaction. Wear **262**, 210–219 (2007)
12. Ben-David, O., Cohen, G., Fineberg, J.: The dynamics of the onset of frictional slip. Science **330**, 211–214 (2010)
13. Ben-David, O., Fineberg, J.: Static friction coefficient is not a material constant. Phys. Rev. Lett. **106**, 254301 (2011)
14. Ben-David, O., Rubinstein, S.M., Fineberg, J.: Slip-stick and the evolution of frictional strength. Nature **463**, 76–79 (2010)
15. Rubinstein, S.M., Cohen, G., Fineberg, J.: Detachment fronts and the onset of dynamic friction. Nature **430**, 1005–1009 (2004)
16. Eriten, M., Polycarpou, A.A., Bergman, L.A.: Physics-based modeling for partial slip behavior of spherical contacts. Int. J. Solids Struct. **47**, 2554–2567 (2010)
17. Wu, A., Shi, X., Polycarpou, A.A.: An elastic–plastic spherical contact model under combined normal and tangential loading. J. Appl. Mech. **79**, 051001 (2012)
18. Mulvihill, D.M., Kartal, M.E., Nowell, D., Hills, D.A.: An elastic–plastic asperity interaction model for sliding friction. Tribol. Int. **44**, 1679–1694 (2011)
19. Greenwood, J.A., Williamson, J.B.P.: Contact of nominally flat surfaces. Proc. R. Soc. Lond. Ser. Math. Phys. Sci. **295**, 300–319 (1966)
20. Kogut, L., Etsion, I.: A static friction model for elastic-plastic contacting rough surfaces. J. Tribol. **126**, 34–40 (2004)
21. Cohen, D., Kligerman, Y., Etsion, I.: A model for contact and static friction of nominally flat rough surfaces under full stick contact condition. J. Tribol. **130**, 31401 (2008)
22. Li, L., Ovcharenko, A., Etsion, I., Talke, F.: The effect of asperity flattening during cyclic normal loading of a rough spherical contact. Tribol. Lett. **40**, 347–355 (2010)
23. Eriten, M., Polycarpou, A.A., Bergman, L.A.: Physics-based modeling for fretting behavior of nominally flat rough surfaces. Int. J. Solids Struct. **48**, 1436–1450 (2011)
24. Lee, C.-H., Eriten, M., Polycarpou, A.A.: Application of elastic-plastic static friction models to rough surfaces with asymmetric asperity distribution. J. Tribol. **132**, 031602 (2010)
25. Björklund, S.: A random model for micro-slip between nominally flat surfaces. J. Tribol. **119**, 726–732 (1997)
26. Yu, N., Polycarpou, A.A.: Contact of rough surfaces with asymmetric distribution of asperity heights. J. Tribol. **124**, 367–376 (2002)
27. McFarlane, J.S., Tabor, D.: Relation between friction and adhesion. Proc. R. Soc. Lond. Ser. Math. Phys. Sci. **202**, 244–253 (1950)
28. ABAQUS Inc: Abaqus Theory Manual. Version V6.12 (2012)
29. McCool, J.I.: Comparison of models for the contact of rough surfaces. Wear **107**, 37–60 (1986)
30. Chandrasekar, S., Eriten, M., Polycarpou, A.A.: An improved model of asperity interaction in normal contact of rough surfaces. J. Appl. Mech. **80**, 011025 (2012)
31. Chang, W.R., Etsion, I., Bogy, D.B.: Static friction coefficient model for metallic rough surfaces. J. Tribol. **110**, 57–63 (1988)
32. Kikuchi, N., Oden, J.T.: Contact problems in elasticity: a study of variational inequalities and finite element methods. SIAM, Philadelphia (1988)
33. Berthe, D., Dowson, D., Godet, M., Taylor, C.M.: Tribological Design of Machine Elements. Elsevier, New York (1989)
34. Stolarski, T.: Tribology in Machine Design. Butterworth-Heinemann, London (1999)
35. Hertz, H.: On the contact of elastic solids. J. Reine Angew. Math. **92**, 110 (1881)
36. Kogut, L., Etsion, I.: Elastic-plastic contact analysis of a sphere and a rigid flat. J. Appl. Mech. **69**, 657–662 (2002)
37. Brizmer, V., Kligerman, Y., Etsion, I.: The effect of contact conditions and material properties on the elasticity terminus of a spherical contact. Int. J. Solids Struct. **43**, 5736–5749 (2006)
38. ABAQUS Inc: Abaqus Analysis User's Manual. Version V6.12 (2012)
39. Perić, D., Owen, D.R.J.: Computational model for 3-D contact problems with friction based on the penalty method. Int. J. Numer. Methods Eng. **35**, 1289–1309 (1992)
40. Biotteau, E., Jean-Philippe, P.: Modeling frictional contact conditions with the penalty method in the extended finite element framework. In: ECCOMAS Proceedings, p. MS119, Vienna, Autriche (2012)
41. Qiu, X., Plesha, M.E., Meyer, D.W.: Stiffness matrix integration rules for contact-friction finite elements. Comput. Methods Appl. Mech. Eng. **93**, 385–399 (1991)
42. Johnson, K.L.: Contact Mechanics. Cambridge University Press, Cambridge (1987)
43. Ashby, M.F., Jones, D.R.H.: Engineering Materials 1: An Introduction to Properties, Applications and Design. Butterworth-Heinemann, New York (2005)
44. MatWeb: Online Materials Information Resource. http://www.matweb.com/
45. Ripling, E.J., Crosley, P.B.: Crack arrest fracture toughness of a structural steel (A36). Weld. Res. 65s–74s (1982)
46. Xue, K., Niu, L.-S., Shi, H.-J.: Mechanical properties of amorphous silicon carbide. In: Mukherjee, M. (ed.) Silicon Carbide—Materials, Processing and Applications in Electronic Devices. pp. 4–22. InTech (2011)
47. Moës, N., Dolbow, J., Belytschko, T.: A finite element method for crack growth without remeshing. Int. J. Numer. Methods Eng. **46**, 131–150 (1999)
48. Baietto, M.C., Pierres, E., Gravouil, A.: A multi-model X-FEM strategy dedicated to frictional crack growth under cyclic fretting fatigue loadings. Int. J. Solids Struct. **47**, 1405–1423 (2010)
49. Giner, E., Sukumar, N., Denia, F.D., Fuenmayor, F.J.: Extended finite element method for fretting fatigue crack propagation. Int. J. Solids Struct. **45**, 5675–5687 (2008)
50. Singh, I.V., Mishra, B.K., Bhattacharya, S., Patil, R.U.: The numerical simulation of fatigue crack growth using extended finite element method. Int. J. Fatigue **36**, 109–119 (2012)
51. Groche, P., Mueller, C., Traub, T., Butterweck, K.: Experimental and numerical determination of roll forming loads. Steel Res. Int. (2013). doi:10.1002/srin.201300190
52. Kirkhorn, L., Frogner, K., Andersson, M., Ståhl, J.E.: Improved tribotesting for sheet metal forming. Procedia CIRP **3**, 507–512 (2012)
53. Bahrami, M., Yovanovich, M.M., Culham, J.R.: Thermal contact resistance at low contact pressure: effect of elastic deformation. Int. J. Heat Mass Transf. **48**, 3284–3293 (2005)
54. Hendriks, C.P., Visscher, M.: Accurate real area of contact measurements on polyurethane. J. Tribol. **117**, 607–611 (1995)
55. Uppal, A.H., Probert, S.D., Thomas, T.R.: The real area of contact between a rough and a flat surface. Wear **22**, 163–183 (1972)

56. Zou, M., Yu, B., Cai, J., Xu, P.: Fractal model for thermal contact conductance. J. Heat Transf. **130**, 101301 (2008)
57. Williamson, J.B.P.: Paper 17: microtopography of surfaces. Proc. Inst. Mech. Eng. Conf. Proc. **182**, 21–30 (1967)
58. Jackson, R.L., Green, I.: A finite element study of elasto-plastic hemispherical contact against a rigid flat. J. Tribol. **127**, 343–354 (2005)
59. Burwell, J.T., Rabinowicz, E.: The nature of the coefficient of friction. J. Appl. Phys. **24**, 136–139 (1953)
60. Ovcharenko, A., Halperin, G., Etsion, I.: Experimental study of adhesive static friction in a spherical elastic-plastic contact. J. Tribol. **130**, 021401 (2008)
61. Marshall, M.B., Lewis, R., Dwyer-Joyce, R.S.: Characterisation of contact pressure distribution in bolted joints. Strain **42**, 31–43 (2006)
62. Stephen, J.T., Marshall, M.B., Lewis, R.: An investigation into contact pressure distribution in bolted joints. Proc. Inst. Mech. Eng. Part C J. Mech. Eng. Sci. 0954406214528320 (2014)
63. Gao, F., Furlong, O., Kotvis, P.V., Tysoe, W.T.: Pressure dependence of shear strengths of thin films on metal surfaces measured in ultrahigh vacuum. Tribol. Lett. **31**, 99–106 (2008)
64. Ibrahim Dickey, R.D., Jackson, R.L., Flowers, G.T.: Measurements of the static friction coefficient between tin surfaces and comparison to a theoretical model. J. Tribol. **133**, 031408 (2011)
65. Zappone, B., Rosenberg, K.J., Israelachvili, J.: Role of nanometer roughness on the adhesion and friction of a rough polymer surface and a molecularly smooth mica surface. Tribol. Lett. **26**, 191–201 (2007)
66. Williams, J.A.: The behaviour of sliding contacts between non-conformal rough surfaces protected by "smart" films. Tribol. Lett. **17**, 765–778 (2004)
67. Zhou, R.S., Hashimoto, F.: A new rolling contact surface and "no run-in" performance bearings. J. Tribol. **117**, 166–170 (1995)
68. Takakuwa, O., Kawaragi, Y., Soyama, H.: Estimation of the yield stress of stainless steel from the Vickers hardness taking account of the residual stress. J. Surf. Eng. Mater. Adv. Technol. **03**, 262–268 (2013)
69. Yu, N., Pergande, S.R., Polycarpou, A.A.: Static friction model for rough surfaces with asymmetric distribution of asperity heights. J. Tribol. **126**, 626–629 (2004)
70. Kim, T.W., Bhushan, B., Cho, Y.J.: The contact behavior of elastic/plastic non-Gaussian rough surfaces. Tribol. Lett. **22**, 1–13 (2006)
71. Kovacevic, R., Mohan, R., Zhang, Y.M.: Cutting force dynamics as a tool for surface profile monitoring in AWJ. J. Manuf. Sci. Eng. **117**, 340–350 (1995)